Eur. Phys. J. Spec. Top. (2026) 235:7209–7218
https://doi.org/10.1140/epjs/s11734-025-02061-5

THE EUROPEAN PHYSICAL JOURNAL SPECIAL TOPICS

Regular Article

Basin entropy and the impact of the escape positioning in an open area-preserving map

Pedro Haerter[1,3,a], Ricardo L. Viana[1,2,b], and Miguel A. F. Sanjuán[3,4,c]

[1] Departamento de Física, Universidade Federal do Paraná, Curitiba 81531-990, Paraná, Brazil
[2] Centro Interdisciplinar de Ciência, Tecnologia e Inovação, Núcleo de Modelagem e Computação Científica, Universidade Federal do Paraná, Curitiba 81531-990, Paraná, Brazil
[3] Nonlinear Dynamics, Chaos, and Complex Systems Group, Departamento de Física, Universidad Rey Juan Carlos, Móstoles 28933, Madrid, Spain
[4] Royal Academy of Sciences of Spain, Valverde 22, Madrid 28004, Spain

Received 25 August 2025 / Accepted 3 November 2025 / Published online 8 November 2025
© The Author(s), under exclusive licence to EDP Sciences, Springer-Verlag GmbH Germany, part of Springer Nature 2025

Abstract Efficient prediction of high-energy particle escape in toroidal fusion devices remains challenging due to the nonlinear dynamics of chaotic magnetic field line trajectories and their extreme sensitivity to initial conditions. Approaches range from comprehensive magnetohydrodynamic models to simplified Hamiltonian mappings. We contribute to bridging this gap by employing a Hamiltonian mapping model of tokamak field lines featuring reversed shear profiles, combined with basin entropy analysis to quantify uncertainty in particle escape locations. Numerical simulations show that strategic positioning of escape exits delays the growth of basin entropy, shifting sharp increases in entropy to higher levels of external perturbation. Our findings illustrate how nonlinear phase space structures can inform the design of plasma-facing components in fusion reactors, significantly improving predictive control of chaotic transport.

1 Introduction

Understanding the escape dynamics of high-energy particles in toroidal fusion devices, such as tokamaks, is critical for effective plasma confinement. However, the inherent nonlinearity of magnetic field line trajectories, which frequently exhibit chaotic and stochastic behavior, present significant challenges [1–3]. These dynamics can be modeled by Hamiltonian systems, in which the volume conservation in the phase space precludes the existence of traditional attractors. Instead, escape basins serve as fundamental tools for analyzing particle transport. Although basins of attraction are well-studied in dissipative systems [4], their counterparts in conservative systems remain relatively underexplored [5–9].

Given a dynamical system, we define a basin of attraction as the set of initial conditions leading to a specific attractor. Hamiltonian dynamical systems, however, do not possess attractors, and consequently, do not have basins of attraction. Moreover, their trajectories can either remain bounded within a closed region in phase space or become unbounded and escape to infinity. When trajectories can escape, we classify the Hamiltonian system as open. In open Hamiltonian systems, we can define an exit or escape basin as the region in phase space containing initial conditions that lead trajectories toward a particular exit. A paradigmatic example illustrating this behavior is provided by the Hénon–Heiles Hamiltonian, in which the system transitions from bounded to open dynamics once the energy surpasses a certain threshold value, commonly termed the escape energy [10]. Above this critical energy, the potential opens up, creating three natural exits through which trajectories may escape to infinity. The same concept can be extended to discrete dynamical systems, also known as area-preserving maps or Hamiltonian maps, where instead of energy, area is conserved. In these systems, the openings can even be introduced artificially, giving rise to various possible configurations [11]. In these systems, the precise placement of escape regions significantly influences the structure and characteristics of the resulting escape basins [12–14].

[a] e-mail: haerter@ufpr.br (corresponding author)
[b] e-mail: viana@fisica.ufpr.br
[c] e-mail: miguel.sanjuan@urjc.es

Previous studies have utilized Hamiltonian maps to analyze chaotic magnetic field-line behavior and particle escape in tokamak devices. However, these works frequently oversimplify the escape mechanisms by defining exit regions arbitrarily, without a physically justified criterion [3, 15, 16]. Specifically, many prior analyses assume escape regions to be homogeneous or position them exclusively near hyperbolic regions in phase space. Such simplifications neglect the complex interplay between nonlinear dynamics and realistic physical boundaries, potentially leading to an incomplete understanding of how escape region placement influences particle transport and basin structures.

This work investigates how the placement of escape regions affects the structure of escape basins and the resulting basin entropy, highlighting the sensitivity of conservative dynamical systems to the configuration of their escape mechanisms. We address these issues through numerical simulations using the revtokamap model, an area-preserving map designed to represent magnetic field lines within toroidal confinement devices, commonly used in plasma fusion experiments [17]. The revtokamap model was specifically chosen for its inclusion of reversed shear dynamics, a key feature in advanced fusion reactors known to significantly reduce turbulent particle transport, thereby enhancing plasma confinement [18]. In contrast to previous studies, which often relied on arbitrarily or simplistically placed escape regions, we systematically vary exit locations within our model. This approach enables us to identify optimal configurations of divertor plates, with the ultimate aim of minimizing chaotic particle transport and thus contributing to improved plasma confinement strategies [19].

In this context, basin entropy plays a crucial role as a quantitative measure for analyzing the complexity and organization of escape basins in the revtokamap model. Basin entropy, which uses Gibbs entropy to quantify uncertainty in escape dynamics, has been particularly effective for detecting subtle structural transitions in basin topology across various dynamical systems. It has been demonstrated to be more sensitive to changes in escape basin structure than traditional nonlinear metrics, such as fractal dimension and the uncertainty exponent [20, 21]. Applying basin entropy to the revtokamap model allows us to assess how varying the exit placement influences the dynamics of magnetic field lines, enabling more informed optimization of divertor configurations and better control of chaotic particle transport in fusion devices.

The motivation for studying the revtokamap model arises from the critical need to better understand the escape of high-energy particles from plasma confinement regions [22, 23]. Such escapes pose significant challenges in tokamaks, as escaping particles can damage plasma-facing components and disrupt confinement, thus threatening overall plasma stability and reactor performance [24]. By systematically introducing and varying escape regions within this model, we can investigate how particle trajectories exit the system and analyze the resulting structural evolution of escape basins under diverse dynamical conditions. Our results demonstrate that strategically positioning escape regions induces abrupt transitions in basin entropy, a phenomenon linked to shifts in particle escape trajectories as external perturbations increase. This insight provides a deeper understanding of the relationship between escape basin complexity and escape mechanism placement, enabling improved predictive control of chaotic transport in fusion plasmas.

The paper is structured as follows: In Sect. 2, we describe the revtokamap model and the numerical methods employed in our analysis. Section 3 investigates how the positioning of escape regions influences basin entropy and the complexity of basin boundaries. Finally, Sect. 4 summarizes the key findings and presents the conclusions of this study.

2 The revtokamap model

Particles of mass m and charge q, in a magnetized tokamak plasma, tend to follow magnetic field lines, describing helical trajectories of gyro-radius $\frac{mv_p}{qB}$, where B is the magnetic field intensity, and v_p is the particle velocity projected on a plane orthogonal to the field direction. If the magnetic field is large enough, we can neglect, in a first approximation, the gyro-motion and assume that the plasma particles follow magnetic field lines. Within this approximation, we also neglect any other drift motions, derived from curvature and inhomogeneities of the

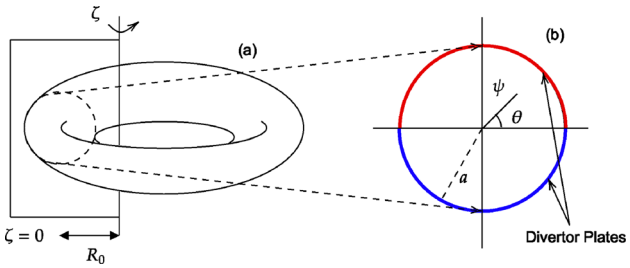


Fig. 1 Schematic figure of **a** a tokamak, **b** a Poincaré surface of section, showing the coordinates used to describe magnetic field lines and the representation of the divertor plates

magnetic field, as well as electric fields. Hence, the magnetic field structure gives a lower-order approximation of the charged particle motion.

Tokamaks are toroidal devices whose goal is the magnetic confinement of fusion plasmas. The tokamak equilibrium magnetic field has two main components: a toroidal field $\mathbf{B}_T$ (created by coils external to the toroidal vessel) and the poloidal field $\mathbf{B}_P$ (due to the plasma current, which is created by induction). The magnetic field lines for $\mathbf{B} = \mathbf{B}_T + \mathbf{B}_P$ have a helical shape and lie on toroidal magnetic surfaces. The so-called magnetic axis is a degenerate magnetic surface.

In Fig. 1a, we represent schematically a toroidal vessel, with minor radius a and major radius R_0. The angle ζ is measured along the toroidal curvature, such that $0 \leq \zeta \leq 2\pi$. If we make a Poincaré surface of section at a plane $\zeta = 0$, the intersection of a magnetic field line can be described by polar coordinates (r, θ), where the origin is the intersection of the magnetic axis with this plane [Fig. 1b]. In this coordinate system, the magnetic surfaces are nested tori with radius $0 \leq r \leq a$ and $0 \leq \theta \leq 2\pi$. We characterize each magnetic surface by a quantity $\psi(r) = \frac{r^2}{a^2}$, in such a way that the magnetic axis and the plasma edge are located at $\psi = 0$ and $\psi = 1$, respectively.

The magnetic field line equations can be expressed as Hamilton's equations, using (ψ, θ) as canonically conjugate variables, and where the angle ζ plays the role of time:

$$\frac{d\psi}{d\zeta} = -\frac{\partial H}{\partial \theta}, \tag{1}$$

$$\frac{d\theta}{d\zeta} = \frac{\partial H}{\partial \psi}, \tag{2}$$

where H is the field line Hamiltonian. In an equilibrium tokamak configuration, due to the axisymmetry, the Hamiltonian does not depend on ζ, and $H(\psi, \theta)$ represents an integrable system. If the latter does not depend on θ, Hamilton's equations are

$$\frac{d\psi}{d\zeta} = 0, \tag{3}$$

$$\frac{d\theta}{d\zeta} = W(\psi), \tag{4}$$

where W is the so-called rotation number, which takes on a constant value on a given magnetic surface.

It turns out that (ψ, θ) are action and angle variables, respectively, such that magnetic surfaces are actually invariant tori of the field line Hamiltonian. Magnetic perturbations which break axisymmetry can be represented by a ζ-dependent Hamiltonian H_1, in such a way that the perturbed field line configuration is described by

$$H(\psi, \theta, \zeta) = H_0(\psi) + H_1(\psi, \theta, \zeta), \tag{5}$$

with $H_0(\psi) = \int_0^{\psi} W(\psi')d\psi'$.

Let us denote by (ψ_n, θ_n) the coordinates of the n-th intersection of a magnetic field line with the plane $\zeta = 0$. We consider a Poincaré map $(\psi_n, \theta_n) \mapsto (\psi_{n+1}, \theta_{n+1})$, relating the coordinates of two consecutive intersections of a field line. The solenoidal condition $\nabla \cdot \mathbf{B} = 0$ implies the conservation of the magnetic flux, and thus the Poincaré map must be area-preserving in the surface of section.

Balescu has proposed an analytical form for the Poincaré map, called revtokamap [17, 25], which is an area-preserving map used to model magnetic field line dynamics in toroidal plasmas exhibiting reversed magnetic shear, a configuration essential for suppressing turbulent transport in fusion devices [26–29]. The map is defined by the following iterative equations:

$$\begin{aligned} \psi_{n+1} &= \frac{1}{2}\left\{ P(\psi_n, \theta_n) + \sqrt{[P(\psi_n, \theta_n)]^2 + 4\psi_n} \right\}, \\ \theta_{n+1} &= \theta_n + W(\psi_{n+1}) - \frac{K}{(2\pi)^2} \frac{\cos(2\pi\theta_n)}{(1+\psi_{n+1})^2}, \end{aligned} \tag{6}$$

where

$$P(\psi_n, \theta_n) = \psi_n - 1 - \frac{K}{2\pi}\sin(2\pi\theta_n), \tag{7}$$

$$W(\psi) = w\left[1 - b(c\psi - 1)^2\right]. \tag{8}$$

Here, ($r \in [0, 1]$) represents the normalized radial coordinate (with ($r = 1$) marking the plasma edge), and ($\theta \in [0, 1)$) is the poloidal angle. The perturbation strength ($K \in [0, 2\pi)$) controls the external perturbation in magnetic field line trajectories, while ($W(\psi)$) governs the winding number profile. By choosing ($W(\psi)$) as a non-monotonic function, the map breaks the twist condition, creating transport barriers that mimic advanced tokamak scenarios [30–32]. We have used as model parameters:

$$b = \frac{w - w_0}{w}, \qquad c = 1 + \left(\frac{w - w_1}{w - w_0}\right)^{1/2}, \tag{9}$$

with $w_0 = 0.3333$, $w = 0.6667$, $w_1 = 0.1667$.

These parameter values were chosen to replicate experimental conditions observed in the DIII-D tokamak experiment [33]. For all numerical simulations, we iterated 1024×1024 initial conditions uniformly distributed across both spatial directions, each evolved for 10^6 iterations.

The area-preserving nature of the revtokamap guarantees Hamiltonian dynamics, making it a computationally efficient alternative to solving complete magnetohydrodynamic equations. Its capability to capture chaotic magnetic field line trajectories and reversed shear effects makes it a robust tool for investigating nonlinear particle transport in fusion plasmas, particularly under conditions involving reversed magnetic shear.

3 Different exit configurations

To explore how different configurations for opening the system influence the dynamical properties of particle escape, we define a particle as escaped when $\psi > 1$. We analyze three distinct exit configurations within the revtokamap:

- **LR case**. It was previously used in [30] and splits the phase space into two exits: $0 \leq \theta < 0.5$, labeled as L (red basins), and $0.5 \leq \theta \leq 1.0$, labeled as R (blue basin), been the simple symmetric division of the phase space into two equal halves.
- **BC case**. Leveraging the periodicity of the angular coordinate θ, a rotation of 90° is applied, resulting in one basin at the boundaries: $(0 \leq \theta < 0.25) \vee (0.75 < \theta \leq 1.0)$, labeled as B (red basin), and another at the center: $0.25 \leq \theta \leq 0.75$, labeled as C (blue basin).
- **Multi case**. This case was designed for a high-resolution analysis of these preferential escape pathways. It divides the escape region into ten contiguous, equally sized basins, each spanning a width of $\Delta\theta = 0.1$. This fine-grained division allows us to resolve the structure of the escape flux in detail.

In this study, rather than using the first iterate outside the boundary as the exit point, we use linear interpolation to determine a more precise exit location, leading to a better classification of the basins [34]. Equation 10 is a standard linear interpolation used to calculate a more precise exit position, at the moment a trajectory crosses the escape boundary at $\psi = 1$. This method is justified because it provides a more accurate classification of the escape basin than simply using the next point outside the boundary. Figure 2 exemplifies how this change can influence the obtained results, and Eq. (10) shows how the points were interpolated

$$\theta_e = \theta_n + (\theta_{n+1} - \theta_n)\frac{1 - \psi_n}{\psi_{n+1} - \psi_n}. \tag{10}$$

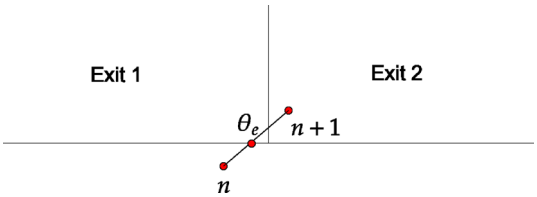


Fig. 2 Representation of the escaping point and how the definition can influence the characterization of a basin. The points n and $n + 1$ represent two iterates of the map, showing the transition between regions. The point θ_e represents the interpolation point calculated using Eq. (10), indicating where the point will escape. This demonstrates that the point should be classified into Basin 1 rather than Basin 2

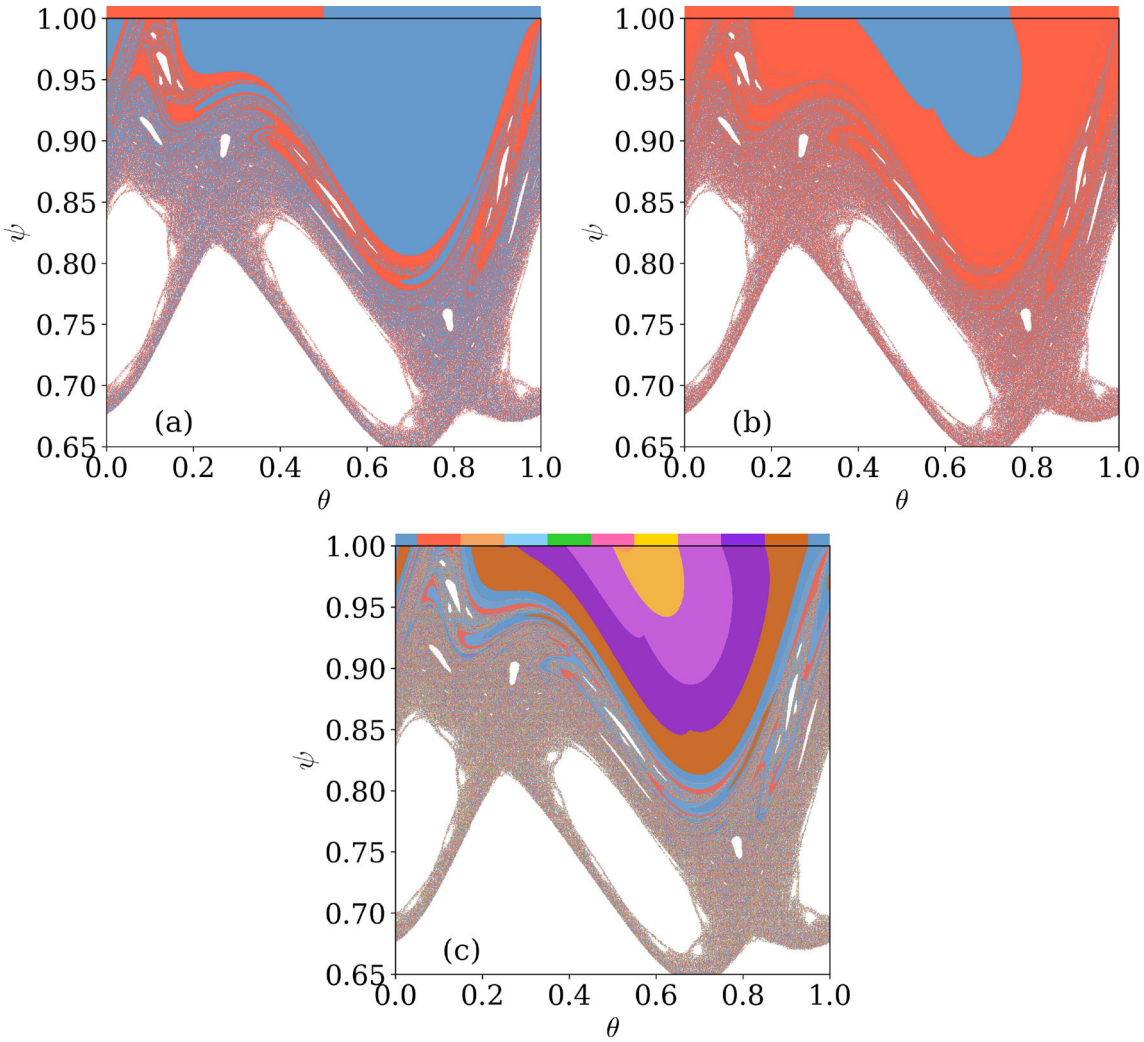


Fig. 3 Escape basins for $K = 2.1$ in the three configurations analyzed: **a** *LR* with the *L* (red) and *R* (blue) exits, **b** *BC* with the *B* (red) and *C* (blue) exits, and **c** *Multi* case, with 10 different exits represented in the figure. The color bar above each plot indicates the corresponding exit region. These plots illustrate clearly how variations in the number and placement of exits alter the structure of escape basins, highlighting preferred regions of escape for this level of perturbation

Figure 3 illustrates how different escape configurations affect the distribution of points within the escape basins, despite maintaining a constant perturbation value across all cases. In the *LR* case, there is a notable intermixing of blue and red basin points near the periodic islands [4, 35], demonstrating significant structural complexity and intertwined basin boundaries.

When the exits are rotated by 90°, the escape basin structure changes substantially, resulting in a clear predominance of the red basin over the blue one. In the *BC* case, most particles escape along the $\theta = \theta_c$ line, with $\theta_c = 0\text{mod}1$, directly impacting the tokamak walls. In practical fusion scenarios, these regions would absorb greater energy fluxes and thus require enhanced protection measures. Although the central region also receives some chaotic particles, most escaping trajectories originate from the same regular region, identifiable as the distinct blue spot.

With this in mind, the *Multi* case positions the blue escape basin along the θ_c line and distributes the remaining nine basins around it, enabling a more detailed analysis of particle escape trajectories. This configuration provides deeper insights, despite the partially Wada nature of the basins previously identified in [30]. A visual inspection of Fig. 3c indicates a high concentration of escaping particles in the blue basin (aligned with the θ_c line) and its adjacent regions (red and dark brown), underscoring areas with preferential particle exits.

To quantify the effects of different exit configurations, we employ basin entropy analysis [20]. This method discretizes a region of interest Ω in the phase space into a grid of boxes, each with a linear size ε. For a given set of parameters, we consider a set of N_A possible exits from this region. With this, it is possible to build a map, $C : \Omega \to \mathbb{N}$, that assigns an exit to each initial condition. This assignment is referred to as the "color."

In principle, each box contains infinitely many trajectories, each leading to a color labeled from 1 to N_A. In practice, only a finite number of trajectories per box can be computed. This number corresponds to the repetitions of an experiment or the number of trajectories calculated in a numerical simulation.

We performed simulations across five different grid resolutions, ranging from a 64×64 to a 1024×1024 grid of initial conditions. For each value of the perturbation parameter K, we then calculated the mean and standard deviation of the entropy values obtained from this set of different simulations. These are then partitioned into N square boxes, where each box contains sixteen initial conditions, we found that this number allows for fast computation while providing accurate values for the basin entropy in all cases studied [20]. This results in a 256×256 grid of boxes. The linear size of one of these boxes, denoted by ε, is therefore $1/256$ and represents our limiting resolution.

Although ε represents our limiting resolution, the information from the trajectories within a box can be used to infer the uncertainty associated with that box. We assume the colors within a box are randomly distributed according to certain proportions. A probability, $p_{i,j}$, can be associated with each color j in a box i. This "probability", or observed frequency, is determined by the statistics of the trajectories originating from that box.

Assuming the trajectories within a box are statistically independent, the *Gibbs* entropy for each box i is given by:

$$S_i = -\sum_{j=1}^{N_A} p_{i,j} \log p_{i,j}, \tag{11}$$

where $p_{i,j}$ is the probability of a color j is the fraction of trajectories from that box that lead to exit j, and we use the convention $0 \ln 0 = 0$.

For a grid of N non-overlapping boxes covering Ω, the total entropy is defined as the sum of the entropies of each individual box:

$$S = \sum_{i=1}^{N} S_i. \tag{12}$$

To create a metric that is independent of the number of boxes (and thus the grid resolution ε), the basin entropy, S_b, is defined as the average entropy per box:

$$S_b = \frac{S}{N}. \tag{13}$$

This concept can be extended to develop other metrics. For instance, we might be interested only in the uncertainty associated with the boundaries between basins. In particular, we often want to know if a boundary is fractal. To this end, we can restrict the entropy calculation to only those boxes that lie on a boundary–that is, the N_b boxes that contain more than one color. This defines the boundary basin entropy, S_{bb}:

$$S_{bb} = \frac{S}{N_b}, \tag{14}$$

which quantifies the uncertainty exclusively at the basin boundaries.

The basin entropy, S_b, quantifies the overall uncertainty of the basins. It ranges from $S_b = 0$ (for a single, predictable outcome) to $S_b = \ln N_A$ (for completely randomized outcomes where all N_A exits are equiprobable). S_b is sensitive to the relative sizes of the basins, allowing it to distinguish between systems with smooth boundaries, whereas S_{bb} is not.

These two quantifiers can be utilized to analyze the complexity, intermingling, and uncertainty of initial conditions within either escape basins or basins of attraction. They are closely related to classical metrics such as the fractal dimension and the uncertainty exponent [20].

Figure 4 displays the solid lines for the basin entropy (S_b) and basin boundary entropy (S_{bb}) representing the mean values from this analysis. The shaded areas depict the corresponding standard deviation, which illustrates the variation in the results across the different grid sizes. Also the occupied basin area for each of the three cases analyzed is presented. As expected, the results across all configurations show that basin entropy increases with larger values of the perturbation parameter. This rise occurs due to enhanced chaotic behavior in the system, leading to greater fractality and complexity of basin structures.

An important observation left unexplained in previous work [30] is the abrupt transition observed in both basin entropy and basin boundary entropy around the critical perturbation value $K_c \approx 2$. This phenomenon is clearly reproduced in our analysis, as illustrated in Fig. 4a. Specifically, basin entropy initially follows a smooth,

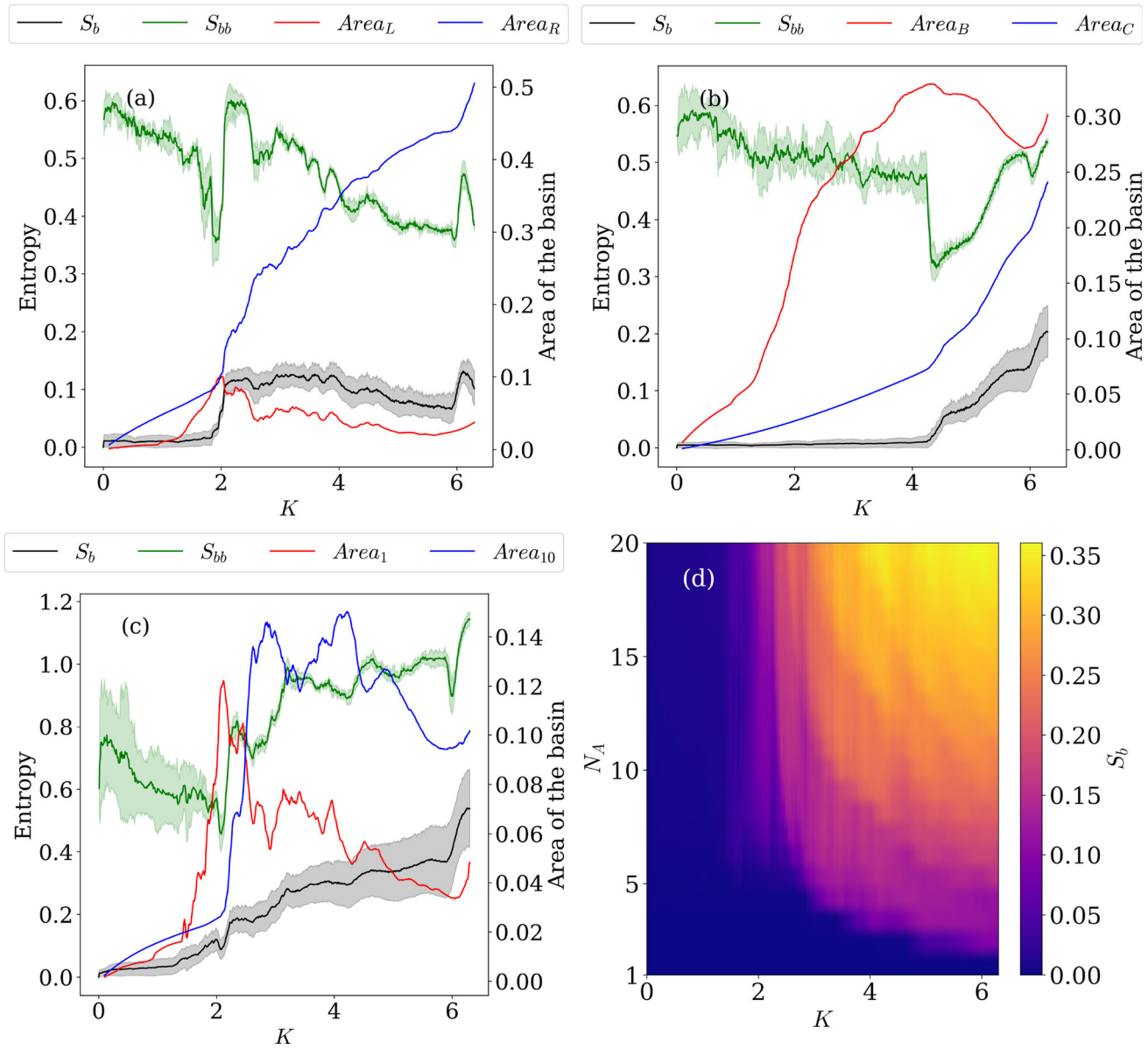


Fig. 4 Mean basin entropy (black), mean basin boundary entropy (green), and basin area fraction as a function of the parameter K for the revtokamap under the three analyzed configurations: **a** *LR* case, **b** *BC* case, and **c** *Multi* case. These plots illustrate the relationships among these measures, highlighting how basin entropy and basin boundary entropy are influenced by changes in occupied basin areas and how all these quantities evolve with increasing perturbation, reflecting greater chaoticity in the system. The effect of different number of exits can be seen in **d**, where the basin entropy is plotted for all the values of K and for all the integers of N_A from 1 to 20

gradually increasing trend at lower perturbation values until reaching the critical point K_c. At this threshold, we observe a sharp, pronounced increase in basin entropy, indicating a sudden structural transition in the escape basin topology. Interestingly, beyond this critical value, basin entropy begins to decrease, suggesting a reorganization or simplification in basin structures as the perturbation further increases. This complex dynamical behavior likely arises from a significant restructuring of chaotic regions and their boundaries, driven by changes in the stability and interactions among invariant sets within phase space.

In Fig. 4a, it is evident that near K_c, the area of the R basin increases abruptly, while the L basin area remains almost constant. This has a direct effect on S_b and S_{bb}, with the highest basin boundary entropy occurring when both areas reach their maximum values. The dominance of one exit over the other, despite the system exhibiting more chaotic behavior due to the increasing perturbation parameter, leads to a decrease in basin entropy.

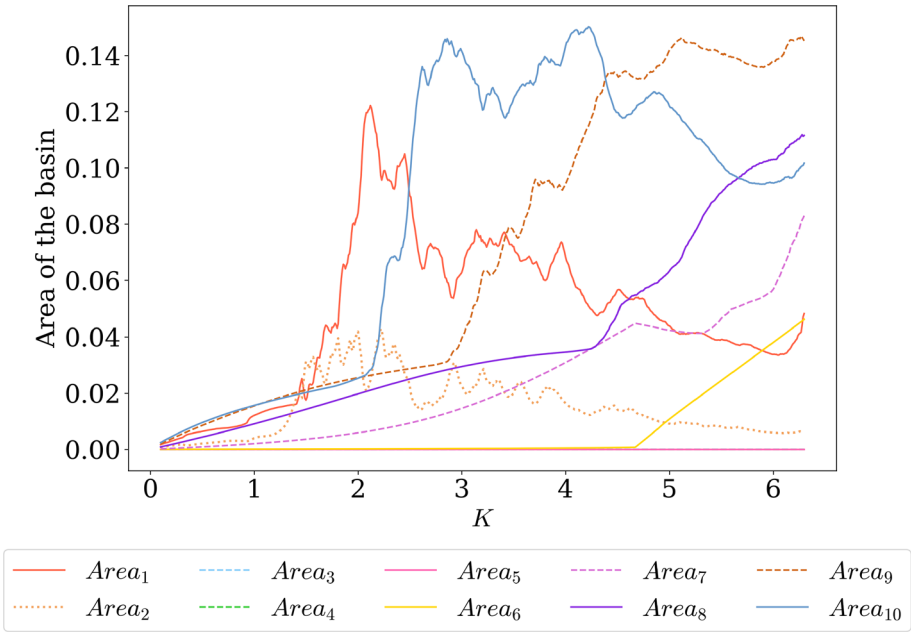


Fig. 5 Areas of the basins for the *Multi* case, with the colors in each area being the ones represented in Fig. 3c

On the other hand, when the exits are moved, as shown in Fig. 3b, the basin entropy in Fig. 4b remains close to zero for higher values of K, with the area of the red basin dominating over the blue one. This persists until a high perturbation value of $K \approx 4$, where the blue basin area begins to increase, and with it, the basin entropy starts to rise. This behavior indicates a preference for escape positions along the θ_c line, which is only altered at high perturbation values.

The *Multi* case deepens our understanding of this phenomenon. By positioning one exit on the θ_c line and analyzing the 10-basin configuration, the preference for particles to escape near the θ_c line becomes clearly demonstrated. Visually, Fig. 3c reveals that even with ten exits available, the basins located in the edge are notably large and more spread, indicating that initial conditions are preferentially channeled toward this border escape region.

This visual preference is confirmed and detailed by the quantitative data in Fig. 5, which plots the individual area of each basin against the perturbation, K. This plot reveals a dynamic shift: for lower values of K, the basin for the first exit, located near θ_c, is dominant, but as K increases past K_c its area decreases while the adjacent $Area_{10}$ basin grows at a similar rate. This "hand-off" between adjacent exits near θ_c shows that the preferred escape route dynamically shifts with increasing chaoticity, which in turn drives the abrupt transitions observed in the basin entropy in Fig. 4c.

4 Conclusions

In this study, we examined how different configurations of openings in a Hamiltonian system influence the escape dynamics, using the revtokamap as our model. This choice was motivated by the revtokamap's realistic representation of magnetic field lines in toroidally confined plasmas, where understanding particle escape mechanisms is critical for improving plasma confinement and reactor performance. The implementation of linear interpolation to better determine the exit points enabled a more accurate classification of escape basins and provided deeper insights into the dynamics of escaping orbits. This methodological approach facilitated the identification of structural transitions and highlighted how basin complexity evolves under varying escape configurations.

By systematically varying the escape configuration across three distinct cases, we characterized how each choice of exits quantitatively and qualitatively impacts escape dynamics. Visual comparisons of escape basin distributions clearly revealed a preferential escape through a specific region aligned along the θ_c line. This observation was further supported by analyzing the basin area fractions, basin entropy, and basin boundary entropy in each configuration, confirming that escape behavior and basin complexity are strongly influenced by the strategic placement and number of exits.

The abrupt changes in basin entropy observed with intuitive phase-space partitions highlight the necessity of accounting for the system's underlying dynamics when defining escape regions. Designing escape regions based on spatial convenience alone can amplify the complexity and unpredictability of the basin structure. A detailed study

of the basin dynamics, for instance by using chaos indicators like SALI [36] to connect the underlying phase space structure to the escape basins, can mitigate this issue.

As the perturbation parameter increases, the shift of particle escape locations near θ_c forces particles to switch between adjacent exit regions, leading to abrupt transitions and greater boundary complexity. These changes disrupt the smoothness of the escape basin boundaries and drive sudden increases in basin mixing. Consequently, as the exit regions become more intermixed, the sharp rise in basin and basin boundary entropy reflects the system's increased unpredictability and structural complexity.

When the exits were moved from the *LR* to the *BC* configuration, the uncertainty in basin structures was significantly suppressed, only becoming prominent at higher perturbation values. This result indicates a more stable exit configuration, which is relevant for identifying regions in fusion devices that may require reinforced plasma-facing components. Additionally, by increasing the number of exits in the *Multi* case, we obtained a more detailed characterization of the escape basin structures. This finer granularity confirmed the presence of preferential escape pathways and highlighted specific regions where escaping particles are most concentrated.

Acknowledgements This work has been supported by grants from the Brazilian Government Agencies CNPq and CAPES. P. Haerter received partial financial support from the following Brazilian government agencies: CNPq (140920/2022-6), CAPES (88887. 898818/2023-00). R. L. Viana received partial financial support from the following Brazilian government agencies: CNPq (403120/2021-7, 301019/2019-3), CAPES (88881. 143103/2017-01). Finally, M. A. F. Sanjuán acknowledges financial support by the Spanish State Research Agency (AEI) and the European Regional Development Fund (ERDF, EU) under Projects No. PID2019-105554GB-I0 (MCIN/AEI/10.13039/501100011033) and No. PID2023-148160NB-I00 (MCIN/AEI/10.13039/501100011033).

Data Availability The data that support the findings of this study are openly available in "Basin entropy and the impact of the escape positioning in an open area-preserving map - CODE" at http://doi.org/10.5281/zenodo.17489213.

References

1. N. Walkden, F. Riva, J. Harrison, F. Militello, T. Farley, J. Omotani, B. Lipschultz, The physics of turbulence localised to the tokamak divertor volume. Commun. Phys. **5**, 139 (2022)
2. S.I. Krasheninnikov, T.K. Soboleva, Dynamics and transport of dust particles in tokamak edge plasmas. Plasma Phys. Control. Fusion **47**, A339 (2005)
3. L.C. Souza, M.R. Sales, M. Mugnaine, J.D. Szezech Jr., I.L. Caldas, R.L. Viana, Chaotic escape of impurities and sticky orbits in toroidal plasmas. Phys. Rev. E **109**, 015202 (2024)
4. A.J. Lichtenberg, M.A. Lieberman, *Regular and Chaotic Dynamics*, Applied Mathematical Sciences, vol. 38. (Springer, New York, 1992)
5. A. Ernst, T. Peters, Fractal basins of escape and the formation of spiral arms in a galactic potential with a bar. Mon. Not. R. Astron. Soc. **443**, 2579–2589 (2014)
6. A. Ernst, A. Just, R. Spurzem, O. Porth, Escape from the vicinity of fractal basin boundaries of a star cluster. Mon. Not. R. Astron. Soc. **383**, 897–906 (2008)
7. E.E. Zotos, Escapes in Hamiltonian systems with multiple exit channels: part I. Nonlinear Dyn. **78**, 1389–1420 (2014)
8. E.E. Zotos, Escapes in Hamiltonian systems with multiple exit channels: part II. Nonlinear Dyn. **82**, 357–398 (2015)
9. E.E. Zotos, Fractal basin boundaries and escape dynamics in a multiwell potential. Nonlinear Dyn. **85**, 1613–1633 (2016)
10. M. Hénon, C. Heiles, The applicability of the third integral of motion: some numerical experiments. Astron. J. **69**, 73–79 (1964)
11. E.G. Altmann, J.S.E. Portela, T. Tél, Leaking chaotic systems. Rev. Mod. Phys. **85**, 869–918 (2013)
12. M.A.F. Sanjuán, T. Horita, K. Aihara, Opening a closed Hamiltonian map. Chaos **13**, 17–24 (2003)
13. J. Schneider, T. Tél, Z. Neufeld, Dynamics of "leaking" Hamiltonian systems. Phys. Rev. E **66**, 066218 (2002)
14. J. Aguirre, J.C. Vallejo, M.A.F. Sanjuán, Wada basins and chaotic invariant sets in the Hénon-Heiles system. Phys. Rev. E **64**, 066208 (2001)
15. A.C. Mathias, L.C. Souza, A.R. Schelin, I.L. Caldas, R.L. Viana, Fractal escape basins for magnetic field lines in fusion plasma devices. J. Appl. Nonlinear Dyn. **12**, 723–738 (2023)
16. L.C. Souza, A.C. Mathias, I.L. Caldas, Y. Elskens, R.L. Viana, Fractal and Wada escape basins in the chaotic particle drift motion in tokamaks with electrostatic fluctuations. Chaos **33**, 083132 (2023)
17. R. Balescu, Hamiltonian nontwist map for magnetic field lines with locally reversed shear in toroidal geometry. Phys. Rev. E **58**, 3781–3792 (1998)
18. S.R. Panta, D.E. Newman, P.W. Terry, R. Sanchez, Control of internal transport barriers in magnetically confined tokamak burning plasmas. Phys. Plasmas **29**, 122503 (2022)
19. A. Loarte, Effects of divertor geometry on tokamak plasmas. Plasma Phys. Control. Fusion **43**, R183 (2001)
20. A. Daza, A. Wagemakers, B. Georgeot, D. Guéry-Odelin, M.A.F. Sanjuán, Basin entropy: a new tool to analyze uncertainty in dynamical systems. Sci. Rep. **6**, 31416 (2016)

21. Á. Daza, A. Wagemakers, M.A.F. Sanjuán, Multistability and unpredictability. Phys. Today **77**, 44–50 (2024)
22. S.J. Zweben, R.A. Ellis, P. Titus, A. Xing, H. Zhang, Rapidly moving divertor plates in a tokamak. Fusion Sci. Technol. **60**, 197–202 (2011)
23. I. Ivanova-Stanik, P. Chmielewski, C. Day, P. Innocente, R. Zagórski, Divertor power spreading in the Divertor Tokamak Test facility for a full power scenario with Ar and Ne seeding. Plasma Phys. Control. Fusion **65**, 055009 (2023)
24. A.C. Mathias, G. Perotto, R.L. Viana, A. Schelin, I.L. Caldas, Fractal structures and magnetic footprints in a divertor tokamak. Int. J. Bifurcation Chaos **32**, 2250078 (2022)
25. R. Balescu, M. Vlad, F. Spineanu, Tokamap: A Hamiltonian twist map for magnetic field lines in a toroidal geometry. Phys. Rev. E **58**, 951–964 (1998)
26. W. Horton, H.-B. Park, J.-M. Kwon, D. Strozzi, P.J. Morrison, D.-I. Choi, Drift wave test particle transport in reversed shear profile. Phys. Plasmas **5**, 3910–3917 (1998)
27. F.M. Levinton, M.C. Zarnstorff, S.H. Batha, M. Bell, R.E. Bell, R.V. Budny, C. Bush, Z. Chang, E.D. Fredrickson, A. Janos, J. Manickam, A. Ramsey, S.A. Sabbagh, G.L. Schmidt, E.J. Synakowski, G. Taylor, Improved confinement with reversed magnetic shear in TFTR. Phys. Rev. Lett. **75**, 4417–4420 (1995)
28. P.W. Terry, Suppression of turbulence and transport by sheared flow. Rev. Mod. Phys. **72**, 109–165 (2000)
29. J.D. Szezech, I.L. Caldas, S.R. Lopes, P.J. Morrison, R.L. Viana, Effective transport barriers in nontwist systems. Phys. Rev. E **86**, 036206 (2012)
30. P. Haerter, L.C. de Souza, A.C. Mathias, R.L. Viana, I.L. Caldas, Basin entropy and Wada property of magnetic field line escape in toroidal plasmas with reversed shear. Int. J. Bifurcation Chaos **33**, 2330022 (2023)
31. L.C. Souza, A.C. Mathias, P. Haerter, R.L. Viana, Basin entropy and shearless barrier breakup in open non-twist Hamiltonian systems. Entropy **25**, 1142 (2023)
32. R.L. Viana, I.L. Caldas, J.D. Szezech Jr., A.M. Batista, C.V. Abud, A.B. Schelin, M. Mugnaine, M.S. Santos, B.B. Leal, B. Bartoloni, J.V. Gomes, P.J. Morrison, Transport barriers in symplectic maps. Braz. J. Phys. **51**, 899–909 (2021)
33. C. M. Greenfield, D. P. Schissel, B. W. Stallard, E. A. Lazarus, G. A. Navratil, K. H. Burrell, T. A. Casper, E. J. Doyle, R. J. Fonck, C. B. Forest, P. Gohil, R. J. Groebner, W. Howl, J. Jackson, R. A. James, R. J. La Haye, L. L. Lao, M. A. Makowski, G. R. McKee, R. A. Moyer, M. Murakami, T. H. Osborne, C. C. Petty, C. L. Rettig, T. L. Rhodes, B. W. Rice, H. E. St. John, R. E. Stockdale, E. J. Strait, E. J. Synakowski, T. S. Taylor, D. M. Thomas, A. D. Turnbull, M. R. Wade, R. Wood, Transport and performance in DIII-D discharges with weak or negative central magnetic shear, Phys. Plasmas 4,1596–1604, (1997)
34. A.C. Mathias, T. Kroetz, I.L. Caldas, R.L. Viana, Chaotic magnetic field lines and fractal structures in a tokamak with magnetic limiter. Chaos, Solitons Fractals **104**, 588–598 (2017)
35. C. Grebogi, E. Ott, J.A. Yorke, Attractors on an N-torus: Quasiperiodicity versus chaos. Physica D **15**, 354–373 (1985)
36. C. Skokos, Alignment indices: a new, simple method for determining the ordered or chaotic nature of orbits. J. Phys. A: Math. Gen. **34**(47), 10029 (2001)

Springer Nature or its licensor (e.g. a society or other partner) holds exclusive rights to this article under a publishing agreement with the author(s) or other rightsholder(s); author self-archiving of the accepted manuscript version of this article is solely governed by the terms of such publishing agreement and applicable law.